Research
High-End Measuring Instruments–Article

A Miniature Meta-Optical System for Reconfigurable Wide-Angle Imaging and Polarization-Spectral Detection

Fei Zhang [a,b,d,†], Minghao Liao [a,b,c,†], Mingbo Pu [a,b,c,d,*], Yinghui Guo [a,b,c,d], Lianwei Chen [a,b,c], Xiong Li [a,b,c], Qiong He [a,b], Tongtong Kang [a,b,d], Xiaoliang Ma [a,b,c], Yuan Ke [e], Xiangang Luo [a,b,c,d,*]

[a] State Key Laboratory of Optical Technologies on Nano-Fabrication and Micro-Engineering, Institute of Optics and Electronics, Chinese Academy of Sciences, Chengdu 610209, China
[b] National Key Laboratory of Optical Field Manipulation Science and Technology, Chinese Academy of Sciences, Chengdu 610209, China
[c] School of Optoelectronics, University of Chinese Academy of Sciences, Beijing 100049, China
[d] Research Center on Vector Optical Fields, Institute of Optics and Electronics, Chinese Academy of Sciences, Chengdu 610209, China
[e] Tianfu Xinglong Lake Laboratory, Chengdu 610299, China

ARTICLE INFO

ABSTRACT

Wide-angle imaging and spectral detection play vital roles in tasks such as target tracking, object classification, and anti-camouflage. However, limited by their intrinsically different architectures, as determined by frequency dispersion requirements, their simultaneous implementation in a shared-aperture system is difficult. Here, we propose a novel concept to realize reconfigurable dual-mode detection based on electrical-control tunable metasurfaces. As a proof-of-concept demonstration, the simultaneous implementation of wide-angle imaging and polarization-spectral detection in a miniature shared-aperture meta-optical system is realized for the first time via the electrical control of cascaded catenary-like metasurfaces. The proposed system supports the imaging (spectral) resolution of approximately 27.8 line-pairs per millimeter (lp·mm^{-1}; ~80 nm) for an imaging (spectral) mode from 8 to 14 μm. This system also bears a large field of view of about 70°, enabling multi-target recognition in both modes. This work may promote the miniaturization of multifunctional optical systems, including spectrometers and polarization imagers, and illustrates the potential industrial applications of meta-optics in biomedicine, security, space exploration, and more.
© 2023 The Authors. Published by Elsevier LTD on behalf of Chinese Academy of Engineering and Higher Education Press Limited Company. This is an open access article under the CC BY-NC-ND license (http://creativecommons.org/licenses/by-nc-nd/4.0/).

1. Introduction

Wide-angle imaging and spectral characterization are two pillars of optical detection with many critical applications, such as target tracking and monitoring, anti-camouflage, and object recognition [1,2]. Many factors can cause the performance of an optical detection system to deteriorate, including artificial camouflage, laser jamming, and severe weather. Thus, a single detection method is often insufficient for accurate target recognition. Hence, there is high demand for multifunctional shared-aperture optical systems [3]. To achieve high imaging and spectral resolution in a broad spectral range, the frequency dispersion of the imager and spectrometer should be suppressed and increased separately, according to the fundamental optical principles associated with refraction, diffraction, and dispersion [4]. However, it is difficult to tune the dispersion of traditional optical materials, because dispersion is determined only by a material's intrinsic molecular or atomic structure [5]. As a result, broadband wide-angle imaging and spectral detection are usually realized by means of two independent systems with different surface curvatures and materials [6], which unavoidably increases the overall size and weight.

Recently, metasurfaces constructed using artificially designed subwavelength structures have been demonstrated to have many unique properties and applications unexploited by conventional optical systems, including multidimensional vectorial optical-field manipulation [7–11], single-chip wide-angle imaging [12–14], tunable multifunctional devices [15–19], holographic information security [20,21], integrated quantum optics [22–24], and asymmetric photonic spin-orbit interactions [25–27], as such metasurfaces can be flexibly manipulated at a local scale in terms of phase, amplitude, and polarization on an ultra-thin plane and lead to generalized laws of reflection and refraction [28–31].

Compared with traditional optical materials such as glasses and crystals, the dispersion of metasurfaces can be flexibly engineered via the geometries of subwavelength structures, thereby enabling applications in broadband imaging [32–37] or spectral detection [38–42] in miniaturized systems. However, the combination of two modes in a shared-aperture system still remains a challenge, because the imaging mode and the spectral detection mode require completely different dispersion characteristics, and the dispersion of a metasurface is fixed once it is fabricated [4].

In this work, we propose the concept of reconfigurable dual-mode detection based on electrical-control tunable metasurfaces, which makes it possible to develop a shared-aperture meta-optical system that is compatible with both broadband wide-angle imaging and polarization-spectral detection. Through the dispersion tunability of electric-control cascaded catenary-like metasurfaces, this proof-of-concept miniature meta-optical system enables fast switching between wide-angle imaging and spin-dependent (circularly polarized) spectral detection modes. The radiation spectra of multiple objects located in a large field of view (FOV) can be simultaneously detected. Here, the term "miniature" is used to indicate that the proposed methodology can theoretically reduce the volume by approximately 50%, because such a shared-aperture system can achieve the functions of two systems. This work aims to provide a new design paradigm for multifunctional optical systems and to promote the practical applications of electrical-control tunable metasurfaces.

2. Methods

2.1. The concept of reconfigurable dual-mode detection

Fig. 1 schematically shows the proposed concept of reconfigurable dual-mode detection based on electrical-control tunable metasurfaces. As shown in Fig. 1(a), the shared-aperture meta-optical system consists of a reconfigurable element for mode switching, a wide-angle lens or metalens for a large FOV, broadband, and diffraction-limited focusing, as well as a sensor for detection. The imaging and spectral modes can be repeatedly and quickly switched from one to another by means of the reconfigurable element, which converts transmitted light between non-diffractive transmission and frequency-spin-dependent diffraction, respectively corresponding to zero and negative frequency dispersion.

The proposed reconfigurable dual-mode detection approach can provide a new route for quick and accurate recognition of moving targets across a large range, including a long distance and a large FOV. When multiple objects are nearby, obtaining their contours by means of the imaging mode is the simplest and most direct way to recognize the target of concern within disruptors; in this case, a large FOV is required, and thus the angular resolution is limited. As shown in Fig. 1(b), when the objects are far away, their images become small and similar on the imaging screen, making the imaging mode invalid, as the angular resolution is insufficient to determine the contours of these objects. Nevertheless, the target can be still distinguished from disruptors such as infrared decoys by means of the circularly polarized radiation spectra obtained in the spectral mode, as shown in Fig. 1(c). In addition, although the appearance and total radiation intensity of the disruptors can easily be falsified to align with the target, the disruptors' radiation spectral characteristics are difficult to camouflage. Furthermore, the spectral mode has a large FOV to simultaneously obtain spatial azimuth angles and polarization spectra of multiple objects for monitoring and tracking. It should be noted that, in this paper, "polarization-spectral detection" refers to the respective detection

of spectra for left-handed and right-handed circularly polarized (LCP and RCP) components.

2.2. Principle of reconfigurability

The key of the proposed reconfigurable element is its conversion between non-diffractive transmission and frequency-spin-dependent diffraction. This can be achieved by means of active liquid crystals, phase-change materials, cascaded metasurfaces, and other materials. Recent studies have illustrated that twisting a bilayer metasurface enables new opportunities for multifunctional devices [43–46]. Here, inspired by catenary optics [14,47], we employ a simple method—that is, two cascaded catenary-like metasurfaces, as illustrated in Figs. 2(a) and (b)—to demonstrate the concept of dual-mode detection. Consider two catenary-like metasurfaces (M1 and M2) that are placed consecutively with the same grating period p but with different angles of θ_1 and θ_2 along the x-direction, respectively. When LCP or RCP light passes through such a reconfigurable element, the wavevector $\boldsymbol{K}_{\text{out}}$ in the transmission can be expressed as follows (see Section S1 in Appendix A for a detailed derivation):

$$
\begin{aligned}
\boldsymbol{K}_{\text{out}} &= \boldsymbol{K}_{\text{in}} + \boldsymbol{G}_1 + \boldsymbol{G}_2 \\
&= (k_0 \sin\xi\cos\varphi \pm \tfrac{k_0\lambda}{p}(\cos\theta_1 - \cos\theta_2), \\
&\quad k_0 \sin\xi\sin\varphi \pm \tfrac{k_0\lambda}{p}(\sin\theta_1 - \sin\theta_2))
\end{aligned}
\tag{1}
$$

where $\boldsymbol{K}_{\text{out}}$ and $\boldsymbol{K}_{\text{in}}$ represent the transverse wavevector of the transmissive and incident light, respectively; $\boldsymbol{G}_1$ and $\boldsymbol{G}_2$ are the transverse wavevectors of the two catenary-like metasurfaces; $k_0 = 2\pi/\lambda$ represents the wavevector of the incident light; λ is the wavelength; ξ is the incident half-FOV angle along the z-direction; φ is the azimuth angle of its projection on the xy-plane; and the $+/-$ sign depends on the spin state of the circularly polarized light. Due to the spin-/polarization-dependent dispersion, the polarization properties can be detected along with the spectral detection, which is helpful in artificial object identification.

To fully collect the transmitted light of the reconfigurable element, a broadband achromatic Fourier lens group consisting of a refractive Fourier lens and a phase meta-corrector is employed, whose effective FOV should be larger than the maximum diffraction angle of both the imaging and spectral modes. Here, a landscape lens design is adopted, and the reconfigurable element is placed at the front of the aperture stop of the lens group. The chromatic aberration of the refractive Fourier lens with positive dispersion is corrected by the phase meta-corrector with negative dispersion. It can be assumed that such an achromatic Fourier lens group allows an ideal focus shift, as follows:

$$
\begin{aligned}
(s_x, s_y) &= f \times \boldsymbol{K}_{\text{out}}/k_0 \\
&= (f \sin\xi\cos\varphi \pm \tfrac{f\lambda}{p}(\cos\theta_1 - \cos\theta_2), \\
&\quad f \sin\xi\sin\varphi \pm \tfrac{f\lambda}{p}(\sin\theta_1 - \sin\theta_2))
\end{aligned}
\tag{2}
$$

where s_x and s_y are the focus shift along the x- and y-directions, respectively; f is the focal length of the achromatic Fourier lens group.

By controlling the rotation angles of θ_1 and θ_2, the reconfigurable element can provide zero and negative frequency dispersion, corresponding to the imaging and spectral modes, respectively. When $\theta_1 = \theta_2$, the focus shift (s_x and s_y) on the image plane is independent of the wavelength and only depends on the half FOV and azimuthal angles of ξ and φ, as illustrated in Fig. 2 (c) (in a special case of $\theta_1 = \theta_2 = 0$ and $\varphi = 0$). In this case, the meta-optical system works as a broadband large-FOV imager. If M1 or M2 is rotated to make $\theta_1 \neq \theta_2$, the incident light rays from the same direction will have a wavelength-spin-dependent focus
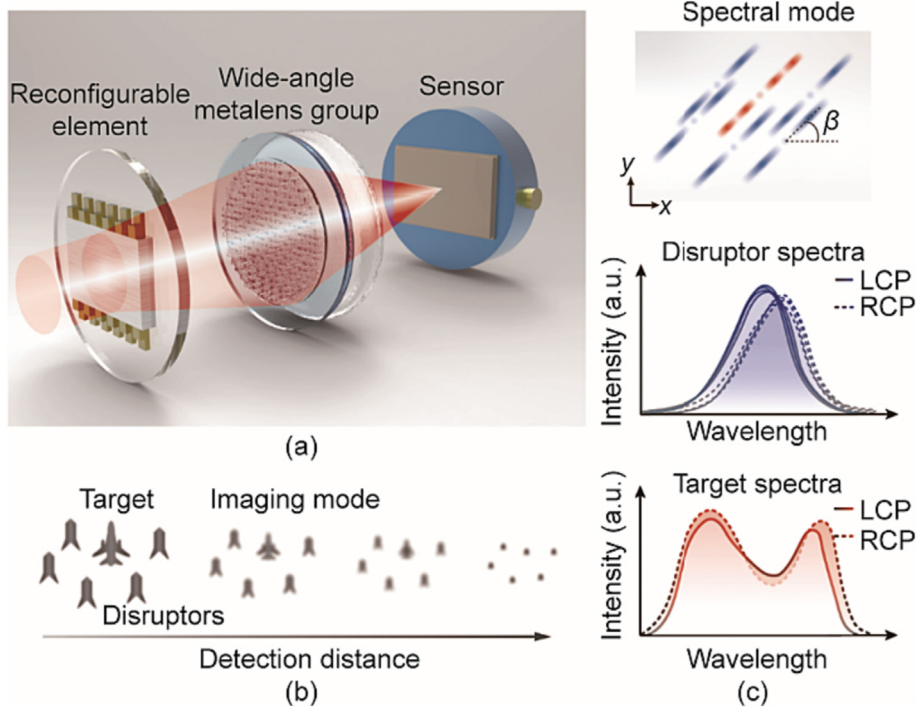
Fig. 1. The concept of reconfigurable dual-mode detection based on electrical-control tunable metasurfaces. (a) Schematic of a shared-aperture meta-optical system, in which the electrical-control reconfigurable element realizes mode switching between wide-angle imaging and spectral detection. (b) Imaging results of disruptors and a target, showing similarities and non-identifiability at a far detection distance. (c) Spectral patterns and polarization radiation spectra of the disruptors and target, with noticeable distinctions. LCP: left-handed circularly polarized; RCP: right-handed circularly polarized; β: the spectral splitting orientation.
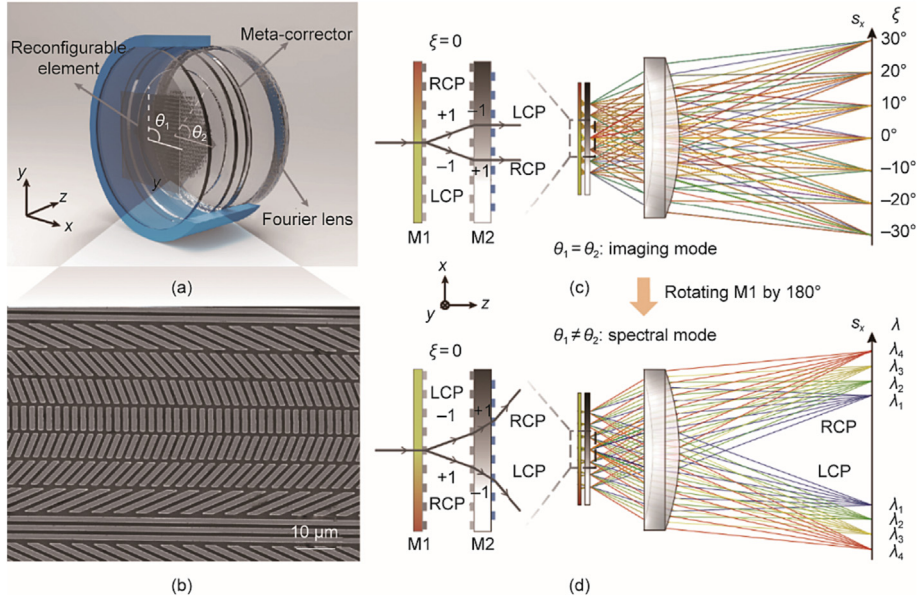

Fig. 2. The principle of reconfigurable wide-angle imaging and polarization-spectral detection. (a) Schematic of the reconfigurable element, which consists of two cascaded catenary-like metasurfaces. (b) Scanning electron microscope image of the catenary-like metasurface. (c) Diagram of the imaging mode in the case of $\theta_1 = \theta_2 = 0$ and $\varphi = 0$. The focus position is only related to the incident half FOV of ξ and the azimuth angle of φ. (d) Diagram of the spectral mode in the case of $\theta_1 = 180°$, $\theta_2 = 0$, $\varphi = 0$, and $\xi = 0$. The left insets of (c) and (d) show the enlarged catenary-like metasurfaces of M1 and M2. The right side of M2 in blue is an eight-step diffractive element for aberration correction. Light rays in different colors represent different wavelengths. s_x: the focus shift along the x-direction; λ_{1-4}: different wavelengths.

shift in the image plane, resulting in a mode switching from the imaging to spectral mode, as displayed in Fig. 2(d) (in the case of $\theta_1 = 180°$, $\theta_2 = 0$, $\varphi = 0$, and $\xi = 0$).

It is concluded from Eq. (2) that the spectral splitting orientation β (illustrated in the top panel of Fig. 1(c)) and the spectral resolution $\Delta\lambda$ can be independently controlled by adjusting the

rotation angles of θ_1 and θ_2, which is conducive to avoiding spectral crosstalk among multiple objects. The spectral splitting orientation of β of the split spectral line along the x-direction is determined by:

$$\beta = \arctan\frac{\mathrm{d}s_y}{\mathrm{d}s_x} = \frac{\theta_1 + \theta_2}{2} - \frac{\pi}{2} \tag{3}$$

According to the Rayleigh criterion, the spectral resolution can be given as follows:

$$\Delta\lambda = \frac{\mathrm{d}\lambda}{\mathrm{d}s}R_{\mathrm{Airy}} = \frac{0.61\lambda p}{D\sin\frac{|\theta_1 - \theta_2|}{2}} \qquad (4)$$

where R_{Airy} indicates the Airy disk radius and D is the effective aperture of the meta-optical system. (See Section S1 for details.)

3. Results and discussion

The proposed concept is universal and can be applied in various spectral bands, such as visible wavelengths for optical monitoring, near-infrared wavelengths for fire prevention and harmful gas detection, or middle- or long-infrared wavelengths for all-weather detection and anti-camouflage. Here, we demonstrate an electric-control reconfigurable meta-optical system operating at a wavelength range from 8 to 14 μm. (See Section S2 in Appendix A for details of the system parameters and performance.) Fig. 3 (a) shows a photograph of our meta-optical system. In this work, we applied a mechanical approach as a simple demonstration of the proposed concept. The switching time between the imaging mode and the spectral mode with the highest resolution was about 1 s. When the reconfigurable element—that is, the combination of two cascaded catenary-like metasurfaces—is replaced by active liquid crystals, phase-change materials, and so forth, the switching time could be reduced to the millisecond or even nanosecond scales. The meta-optical system has a focal length of 11.5 mm, an effective diameter of 5 mm, and a near-diffraction-limited FOV of 60° × 60°. The sensor has 1024 × 1280 pixels with a pixel size of 12 μm. The two catenary-like metasurfaces have a period of 17 line-pairs per millimeter (lp·mm^{-1}). (See Section S3 in Appendix A for details of the metasurface design; a scanning electron microscope image is shown in Fig. 2(b).) The simulated average

diffraction efficiency within 8–14 μm reached about 93%, while the measured diffraction efficiency reached about 85% at 10.6 μm, due to fabrication errors. The diffraction efficiency is defined as the ratio of the diffraction order power to the total transmitted power. (See Section S4 in Appendix A for details of sample fabrications and experimental setups.)

To test the performance of the imaging mode, the imaging resolution and FOV of the meta-optical system were characterized. A 1951 US Air Force (USAF) resolution test chart was used to characterize the imaging resolution. Fig. 3(b) shows an image of the USAF resolution test chart captured at an object distance of approximately 150 mm. The modulation transform function (MTF) curves of the meta-optical system are shown in Fig. 3(c), including the diffraction limit, simulated MTF by the ray-tracing method, and experimental results. Eight elements from 12.8 to 27.8 lp·mm^{-1} were characterized against the theoretically predicted value. The insets display the images of the three line-pairs. Furthermore, the simulated spot diagrams at different wavelengths (see Section S2) reveal that all light rays are within their corresponding Airy disks, showing the near-diffraction-limited focusing performance. The meta-optical system supports an FOV of approximately 76° and 61° along the horizontal and vertical (see Section S5 in Appendix A). Fig. 3(d) shows an image of an outdoor environment captured by the meta-optical system, demonstrating its good imaging performance and large FOV.

Subsequently, spin-dependent spectral detection was demonstrated by characterizing the transmission spectra of several infrared filters and a silicon wafer. In the following, the spectral resolution was set at the highest level ($|\theta_1 - \theta_2| = 180°$). As shown in Fig. 4(a), the spectral resolution ranges from approximately 60 to 100 nm within 8–14 μm. (The tunable spectral resolution is demonstrated in Section S6 in Appendix A.) The calibration of the spectral mode was carried out with an adjustable carbon dioxide laser to make the spectral detection more accurate. The calibration
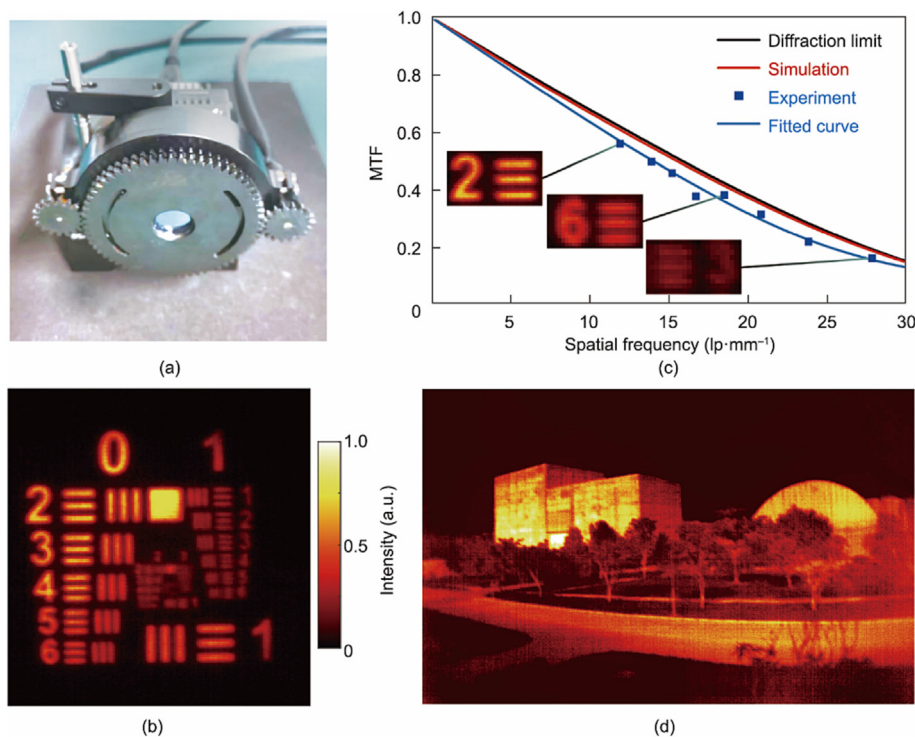

Fig. 3. Large-FOV thermal imaging results captured by an infrared electric-control meta-optical system in the imaging mode. (a) Photograph of the meta-optical system. (b) Image of the US Air Force (USAF) resolution test chart. (c) Simulated and measured MTF curves. Discrete points and insets are experimental results, showing good consistency with simulation results. (d) Thermal image of an outdoor environment. MTF: modulation transform function.
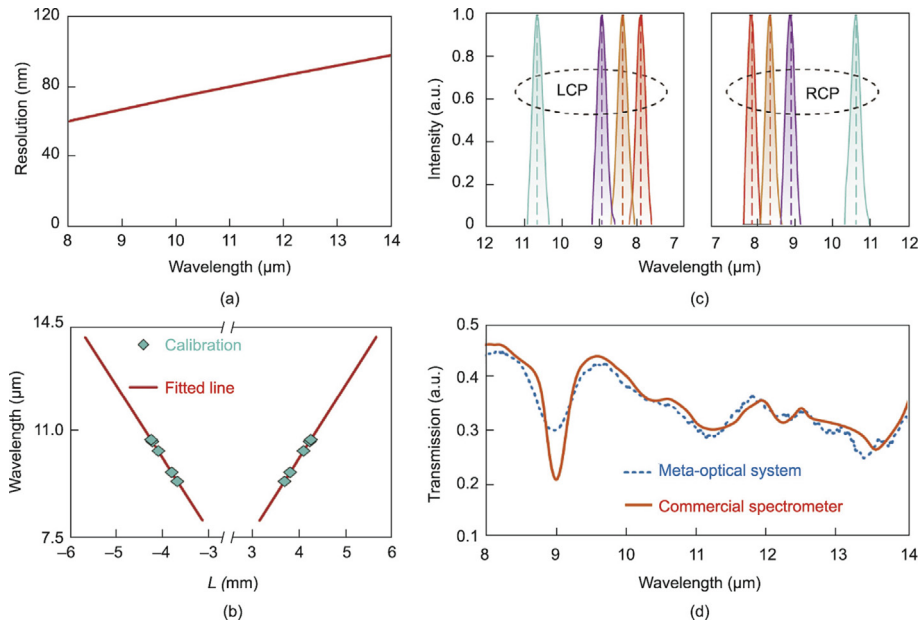
F. Zhang, M. Liao, M. Pu et al.

Fig. 4. Spectral detection results measured by the infrared electric-control meta-optical system in the spectral mode. (a) Simulated spectral resolution; (b) calibration results of the relationship between the projection position L and the wavelength; (c) measured transmission spectra of four optical filters; (d) measured transmission spectrum of a silicon slice. The red and blue curves are obtained by a commercial Fourier spectrometer and our meta-optical system, respectively. L: the distance between the spectral pattern and the zero-order focus.

result is shown in Fig. 4(b). The zero-order focus is defined as the origin. The projection positions at different wavelengths were tested and then linearly fitted to obtain $\lambda = \pm 2.401L \times 10^{-3} + 4.296 \times 10^{-7}$ for RCP and LCP light, respectively, where L is the distance between the spectral pattern and the zero-order focus.

Fig. 4(c) presents the normalized spectral results of a series of infrared filters. The red, orange, purple, and green represent central wavelengths of 7.85, 8.33, 8.85, and 10.6 μm, respectively. Since

our thermal source is non-polarized, spectral curves exhibit good mirror symmetry. (See Section S7 in Appendix A for details on polarization-dependent spectral detection.) The measured central wavelengths have tiny deviations (∼0.3%) against the marked central wavelengths (dotted lines) of the infrared filters, which mainly result from the quantization error. The 12 μm pixel size of the detector corresponds to a spectrum width of about 30.7 nm. Fig. 4(d) shows a measured transmission spectrum of a double-
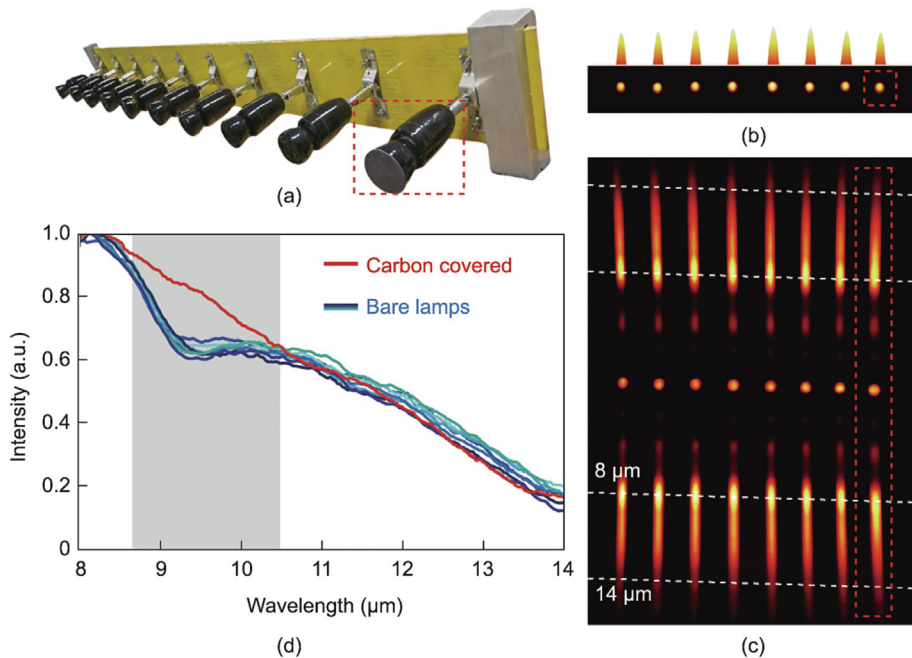

Fig. 5. Multi-target thermal-radiation spectral detection, validating the ability to identify the red-square-marked real target from disruptors. (a) Intensity image captured in the imaging mode, showing the indistinguishability of the real target in the imaging mode. The top panel shows the corresponding intensity profile. (b) Spectral patterns captured in the spectral mode. White dashed lines indicate the cutoff wavelengths of 8 μm and 14 μm. (c) Experimental layout of the ceramic lamp array, in which a carbon-covered ceramic lamp is employed to simulate the real target with a different radiation spectrum. (d) Normalized spectra of bare and carbon-covered ceramic lamps, with different features marked with a gray area.

polished silicon wafer with a thickness of about 1.5 mm. The red and blue curves were obtained using a commercial Fourier spectrometer (Bruker VERTEX 80v, Bruker, Germany) and the meta-optical system, respectively, and show good agreement. The main valley at a wavelength of approximately 9.1 μm resulting from the absorption of the silicon is widened because of the relatively large size of the thermal source. Other deviations mainly come from the thermal noise and the nonlinear response of the employed uncooled infrared detector.

Finally, multi-target thermal radiation spectral detection was demonstrated via a row of ceramic lamps, as shown in Fig. 5(a). One of the lamps (marked with a red square) was covered with a carbon plate to simulate a real target producing a different thermal radiation spectrum from the other bare lamps. Fig. 5(b) shows the image of the lamps and the corresponding intensity profile in the imaging mode. The images are very similar in contour, size, and intensity, making the carbon-covered ceramic lamp indistinguishable from the rest. Fig. 5(c) shows the spectral patterns of these ceramic lamps. The large FOV allows for the complete separation and independence of light from different sources, enabling simultaneous detection of the entire object. White dashed lines indicate the cutoff wavelengths of 8 and 14 μm. Since these ceramic lamps are not strictly parallel to the horizontal direction of the meta-optical system, these lines are not parallel to the edge of the figure but are proximately parallel to the central imaging patterns that contribute to the zero-order diffraction of the two catenary-like metasurfaces. It should be mentioned that, due to the existence of the zero-order diffraction caused by fabrication errors, the combination of the first-order and zero-order diffraction respectively generated by two catenary-like metasurfaces cause extra spectral patterns between the central imaging patterns and the 8 μm boundary of the main spectral patterns. The spectra of those bare ceramic lamps are drawn in blue in Fig. 5(d), while the spectrum of the carbon-covered ceramic lamp is presented as a red curve, exhibiting a noticeable difference in the shaded gray area. This property enables the recognition of the target that cannot be differentiated in the imaging mode, which holds great importance for enhancing target tracking and recognition.

4. Conclusions

In summary, we reported the concept of reconfigurable dual-mode detection based on electrical-control tunable metasurfaces. Broadband large-FOV imaging and circularly polarized spectral detection were implemented by means of a shared-aperture meta-optical system for the first time. As a proof-of-concept demonstration, via the electrical control of cascaded catenary-like metasurfaces, an infrared miniature electrical-control meta-optical system was experimentally demonstrated with the abilities of near-diffraction-limited imaging, spectral detection, and multi-target recognition. This concept can be expanded to visible, near-infrared, mid-infrared, or other bands for broader applications.

This work may provide a new way to integrate multiple functions within a single miniature shared-aperture system, which is of great importance in the fields of object classification and anti-camouflage, as it opens up new avenues for various applications, such as the quick and accurate recognition of moving targets across a large range. In addition, active liquid crystals and phase-change materials can be directly employed to construct such reconfigurable systems with a high switching speed and no mechanical movement. The imaging and spectral resolution can be improved by increasing the effective diameter, although this may increase the number of lenses. At the same time, the FOV can be increased by adding more lenses. Furthermore, translating the two cascaded catenary-like metasurfaces can change the corresponding output polarization state and thus achieve polarization imaging after a polarization filter is inserted behind them.

Compliance with ethics guidelines

Fei Zhang, Minghao Liao, Mingbo Pu, Yinghui Guo, Lianwei Chen, Xiong Li, Qiong He, Tongtong Kang, Xiaoliang Ma, Yuan Ke, and Xiangang Luo declare that they have no conflict of interest or financial conflicts to disclose.

Appendix A. Supplementary data

Supplementary data to this article can be found online at https://doi.org/10.1016/j.eng.2023.07.008.

References

[1] Goetz AF, Vane G, Solomon JE, Rock BN. Imaging spectrometry for Earth remote sensing. Science 1985;228(4704):1147–53.
[2] He L, Li J, Liu C, Li S. Recent advances on spectral-spatial hyperspectral image classification: an overview and new guidelines. IEEE Trans Geosci Remote Sens 2018;56(3):1579–97.
[3] Shimoni M, Haelterman R, Perneel C. Hypersectral imaging for military and security applications: combining myriad processing and sensing techniques. IEEE Geosci Remote Sens Mag 2019;7(2):101–17.
[4] Chen WT, Zhu AY, Capasso F. Flat optics with dispersion-engineered metasurfaces. Nat Rev Mater 2020;5(8):604–20.
[5] Li X, Pu M, Ma X, Guo Y, Gao P, Luo X. Dispersion engineering in metamaterials and metasurfaces. J Phys D Appl Phys 2018;51(5):054002.
[6] Zou X, Zheng G, Yuan Q, Zang W, Chen R, Li T, et al. Imaging based on metalenses. PhotoniX 2020;1:2.
[7] He C, Shen Y, Forbes A. Towards higher-dimensional structured light. Light Sci Appl 2022;11:205.
[8] Liu M, Huo P, Zhu W, Zhang C, Zhang S, Song M, et al. Broadband generation of perfect Poincaré beams via dielectric spin-multiplexed metasurface. Nat Commun 2021;12:2230.
[9] Deng ZL, Tu QA, Wang Y, Wang ZQ, Shi T, Feng Z, et al. Vectorial compound metapixels for arbitrary nonorthogonal polarization steganography. Adv Mater 2021;33(43):e2103472.
[10] Bao Y, Wen L, Chen Q, Qiu CW, Li B. Toward the capacity limit of 2D planar Jones matrix with a single-layer metasurface. Sci Adv 2021;7(25):eabh0365.
[11] Zhang F, Pu M, Guo Y, Ma X, Li X, Gao P, et al. Synthetic vector optical fields with spatial and temporal tunability. Sci China-Phys Mech Astron 2022;65(5):254211.
[12] Chen J, Ye X, Gao S, Chen Y, Zhao Y, Huang C, et al. Planar wide-angle-imaging camera enabled by metalens array. Optica 2022;9(4):431–7.
[13] Martins A, Li K, Li J, Liang H, Conteduca D, Borges BHV, et al. On metalenses with arbitrarily wide field of view. ACS Photonics 2020;7(8):2073–9.
[14] Zhang F, Pu M, Li X, Ma X, Guo Y, Gao P, et al. Extreme-angle silicon infrared optics enabled by streamlined surfaces. Adv Mater 2021;33(11):e2008157.
[15] Shalaginov MY, An S, Zhang Y, Yang F, Su P, Liberman V, et al. Reconfigurable all-dielectric metalens with diffraction-limited performance. Nat Commun 2021;12:1225.
[16] Wan X, Xiao C, Huang H, Xiao Q, Xu W, Li Y, et al. Joint modulations of electromagnetic waves and digital signals on a single metasurface platform to reach programmable wireless communications. Engineering 2022;8:886–95.
[17] Meng W, Hua Y, Cheng K, Li B, Liu T, Chen Q, et al. 100 hertz frame-rate switching three-dimensional orbital angular momentum multiplexing holography via cross convolution. Opto-Electron Sci 2022;1(9):220004.
[18] Li J, Yu P, Zhang S, Liu N. A reusable metasurface template. Nano Lett 2020;20(9):6845–51.
[19] Wang ZX, Yang H, Shao R, Wu JW, Liu G, Zhai F, et al. A planar 4-bit reconfigurable antenna array based on the design philosophy of information metasurfaces. Engineering 2022;17:64–74.
[20] Zheng P, Dai Q, Li Z, Ye Z, Xiong J, Liu HC, et al. Metasurface-based key for computational imaging encryption. Sci Adv 2021;7(21):eabg0363.
[21] Georgi P, Wei Q, Sain B, Schlickriede C, Wang Y, Huang L, et al. Optical secret sharing with cascaded metasurface holography. Sci Adv 2021;7(16):eabf9718.

F. Zhang, M. Liao, M. Pu et al.

[22] Santiago-Cruz T, Gennaro SD, Mitrofanov O, Addamane S, Reno J, Brener I, et al. Resonant metasurfaces for generating complex quantum states. Science 2022;377(6609):991–5.

[23] Liu J, Shi M, Chen Z, Wang S, Wang Z, Zhu S. Quantum photonics based on metasurfaces. Opto-Electron Adv 2021;4(9):200092.

[24] Li L, Liu Z, Ren X, Wang S, Su VC, Chen MK, et al. Metalens-array-based high-dimensional and multiphoton quantum source. Science 2020;368 (6498):1487–90.

[25] Cai J, Zhang F, Pu M, Chen Y, Guo Y, Xie T, et al. Dispersion-enabled symmetry switching of photonic angular-momentum coupling. Adv Funct Mater 2023;33 (19):2212147.

[26] Devlin RC, Ambrosio A, Rubin NA, Mueller JPB, Capasso F. Arbitrary spin-to-orbital angular momentum conversion of light. Science 2017;358 (6365):896–901.

[27] Zhang F, Pu M, Li X, Gao P, Ma X, Luo J, et al. All-dielectric metasurfaces for simultaneous giant circular asymmetric transmission and wavefront shaping based on asymmetric photonic spin-orbit interactions. Adv Funct Mater 2017;27(47):1704295.

[28] Song Q, Odeh M, Zúñiga-Pérez J, Kanté B, Genevet P. Plasmonic topological metasurface by encircling an exceptional point. Science 2021;373 (6559):1133–7.

[29] Xie X, Pu M, Jin J, Xu M, Guo Y, Li X, et al. Generalized pancharatnam-berry phase in rotationally symmetric meta-atoms. Phys Rev Lett 2021;126 (18):183902.

[30] Yu N, Genevet P, Kats MA, Aieta F, Tetienne JP, Capasso F, et al. Light propagation with phase discontinuities: generalized laws of reflection and refraction. Science 2011;334(6054):333–7.

[31] Luo X. Principles of electromagnetic waves in metasurfaces. Sci China Phys Mech Astron 2015;58(9):594201.

[32] Wang Y, Chen Q, Yang W, Ji Z, Jin L, Ma X, et al. High-efficiency broadband achromatic metalens for near-IR biological imaging window. Nat Commun 2021;12:5560.

[33] Ou K, Yu F, Li G, Wang W, Miroshnichenko AE, Huang L, et al. Mid-infrared polarization-controlled broadband achromatic metadevice. Sci Adv 2020;6 (37):eabc0711.

[34] Zhou H, Chen L, Shen F, Guo K, Guo Z. Broadband achromatic metalens in the midinfrared range. Phys Rev Appl 2019;11(2):024066.

[35] Chen WT, Zhu AY, Sanjeev V, Khorasaninejad M, Shi Z, Lee E, et al. A broadband achromatic metalens for focusing and imaging in the visible. Nat Nanotechnol 2018;13(3):220–6.

[36] Wang S, Wu PC, Su VC, Lai YC, Chen MK, Kuo HY, et al. A broadband achromatic metalens in the visible. Nat Nanotechnol 2018;13(3):227–32.

[37] Wang Y, Fan Q, Xu T. Design of high efficiency achromatic metalens with large operation bandwidth using bilayer architecture. Opto-Electron Adv 2021;4:200008.

[38] Yang Z, Albrow-Owen T, Cai W, Hasan T. Miniaturization of optical spectrometers. Science 2021;371(6528):eabe0722.

[39] McClung A, Samudrala S, Torfeh M, Mansouree M, Arbabi A. Snapshot spectral imaging with parallel metasystems. Sci Adv 2020;6(38):eabc7646.

[40] Faraji-Dana M, Arbabi E, Arbabi A, Kamali SM, Kwon H, Faraon A. Compact folded metasurface spectrometer. Nat Commun 2018;9:4196.

[41] Yoon HH, Fernandez HA, Nigmatulin F, Cai W, Yang Z, Cui H, et al. Miniaturized spectrometers with a tunable van der Waals junction. Science 2022;378 (6617):296–9.

[42] Deng W, Zheng Z, Li J, Zhou R, Chen X, Zhang D, et al. Electrically tunable two-dimensional heterojunctions for miniaturized near-infrared spectrometers. Nat Commun 2022;13:4627.

[43] Hu G, Wang M, Mazor Y, Qiu CW, Alù A. Tailoring light with layered and Moiré metasurfaces. Trends Chem 2021;3(5):342–58.

[44] Hu G, Krasnok A, Mazor Y, Qiu CW, Alù A. Moiré hyperbolic metasurfaces. Nano Lett 2020;20(5):3217–24.

[45] Wang P, Zheng Y, Chen X, Huang C, Kartashov YV, Torner L, et al. Localization and delocalization of light in photonic Moiré lattices. Nature 2020;577 (7788):42–6.

[46] Hu G, Ou Q, Si G, Wu Y, Wu J, Dai Z, et al. Topological polaritons and photonic magic angles in twisted α-MoO₃ bilayers. Nature 2020;582(7811):209–13.

[47] Pu M, Li X, Ma X, Wang Y, Zhao Z, Wang C, et al. Catenary optics for achromatic generation of perfect optical angular momentum. Sci Adv 2015;1(9):e1500396.